

# Journal of Biomedical Optics

BiomedicalOptics.SPIEDigitalLibrary.org

## **Raman mapping of oral buccal mucosa: a spectral histopathology approach**

Isha Behl  
Lekha Kukreja  
Atul Deshmukh  
S. P. Singh  
Hitesh Mamgain  
Arti R. Hole  
C. Murali Krishna

# Raman mapping of oral buccal mucosa: a spectral histopathology approach

Isha Behl,<sup>a</sup> Lekha Kukreja,<sup>a</sup> Atul Deshmukh,<sup>a</sup> S. P. Singh,<sup>a</sup> Hitesh Mamgain,<sup>b</sup> Arti R. Hole,<sup>a</sup> and C. Murali Krishna<sup>a,\*</sup>

<sup>a</sup>Chilakapati Lab, ACTREC, Kharghar, Navi-Mumbai 410210, India

<sup>b</sup>WITec GmbH, Lisemeitner-str.6, D-89081 Ulm, Germany

**Abstract.** Oral cancer is one of the most common cancers worldwide. One-fifth of the world's oral cancer subjects are from India and other South Asian countries. The present Raman mapping study was carried out to understand biochemical variations in normal and malignant oral buccal mucosa. Data were acquired using WITec alpha 300R instrument from 10 normal and 10 tumors unstained tissue sections. Raman maps of normal sections could resolve the layers of epithelium, i.e. basal, intermediate, and superficial. Inflammatory, tumor, and stromal regions are distinctly depicted on Raman maps of tumor sections. Mean and difference spectra of basal and inflammatory cells suggest abundance of DNA and carotenoids features. Strong cytochrome bands are observed in intermediate layers of normal and stromal regions of tumor. Epithelium and stromal regions of normal cells are classified by principal component analysis. Classification among cellular components of normal and tumor sections is also observed. Thus, the findings of the study further support the applicability of Raman mapping for providing molecular level insights in normal and malignant conditions. © 2014 Society of Photo-Optical Instrumentation Engineers (SPIE) [DOI: [10.1117/1.JBO.19.12.126005](https://doi.org/10.1117/1.JBO.19.12.126005)]

Keywords: oral cancer; Raman spectroscopy; Raman mapping; principal component analysis.

Paper 140249PRR received Apr. 18, 2014; accepted for publication Oct. 30, 2014; published online Dec. 5, 2014.

## 1 Introduction

Cancer is the second most common cause of morbidity and mortality in the world today, after cardiovascular disorders. There were an estimated 14.1 million cancer cases around the world in 2012; of these 7.4 million cases were in men and 6.7 million were in women.<sup>1</sup> This number is expected to increase to 24 million by 2035. Squamous cell carcinoma of the oral cavity ranks as the 15th most common cancer in the world and 10th most frequent in males.<sup>1</sup> The Indian subcontinent accounts for one-third of the global burden.<sup>2</sup> Buccal mucosa is known to be the most common site contributing ~57% of all cases followed by the lateral surface of the tongue (24%).<sup>3</sup> This can be attributed to the wide spread use of chewable tobacco which is generally placed in the buccal or lingual vestibule.<sup>2</sup> It is also reported that tobacco-related cancers accounts for ~42% of Indian male and 18% of Indian female cancer-related deaths.<sup>1</sup>

Normal buccal mucosa is a non-keratinized stratified squamous epithelium, comprises stratum basale (basal), stratum intermedium (intermediate), and stratum superficiale (superficial) layers followed by connective tissue. Oral squamous cell carcinoma (OSCC) causes structural loss in the stratification of epithelium, subsequent invasion, and infiltration of malignant epithelial cells into the connective tissue.<sup>4</sup> Presently, the gold standard for the assessment of oral malignancy is microscopic evaluation of hematoxylin and eosin (HE) stained tissue sections. It combines architectural, cytological, and arrangements of epithelial strata changes for the diagnosis and grading of oral cancers. However, this method is time consuming and prone to inter/intra-observer variations. Moreover, the

diagnostic accuracy also depends on the precision of the resected biopsy material that represents the actual suspected lesion.

Optical spectroscopic methodologies are being explored as alternates/adjuncts to existing diagnostic tools. These methods are label free as they do not require the usage of external agents such as dyes, stains, or radioactive labels. The efficacy of optical spectroscopic techniques such as fluorescence, Raman and Fourier-transform infrared (FTIR) spectroscopy in classifying normal and pathological conditions has already been demonstrated.<sup>5-7</sup> Raman spectroscopic methods are based on the inelastic scattering of light. It is an ideal method for *in vivo* applications, due to the attributes like negligible water interference, sharp spectral signatures, and abundance of active species in biological samples. In fact, fiberoptic Raman studies in detection of oral cancers and its confounding factors have already been demonstrated.<sup>8-11</sup>

Raman mapping is another approach for obtaining molecular level information of tissue sections using Raman microspectroscopy. Histopathology is a morphological representation of the tissue in question and does not signify the underlying biochemical changes. Raman maps, on the other hand, are sensitive to biochemical changes in tissue sections. Raman microspectroscopy of biological molecules has been reported as early as 1990.<sup>12</sup> It was followed by another pioneer study in 1997 by Gniadecka et al.<sup>13</sup> on basal cell carcinoma (BCC). In 2002, Annieke Nijssen et al.<sup>14</sup> explored the possibility of determining tumor margins by using Raman mapping. Unlike Gniadecka et al. unfixed thin tissue sections were used to identify specific spectral information on BCC, peritumoral dermal connective tissue, and epidermis through Raman maps. Based on this

\*Address all correspondence to: C. Murali Krishna, Email: [mchilakapati@actrec.gov.in](mailto:mchilakapati@actrec.gov.in) or [pittu1043@gmail.com](mailto:pittu1043@gmail.com)

information, a prediction model was constructed for spectra obtained from BCC, dermis, and epidermis. There have been several studies reported on differentiation of normal, precancerous, and malignant tissues on the basis of the distribution of biomolecules. The findings of most of these studies are suggestive of the fact that Raman mapping can serve as an adjuvant technique providing molecular insight along with routine HE examination.<sup>15–22</sup>

Previous Raman spectroscopic studies have shown that pre-malignant lesions and various confounding factors associated with oral cancers can be objectively discriminated under *in-vivo* conditions.<sup>9,10</sup> Oral mucosa is heterogeneous in nature and comprises different layers and histological features. To understand the pathophysiology of the underlying epithelium-related changes during (pre)-malignant transformation, it is essential to explore the biochemical changes along with the morphological architecture of the tissue. Thus, the mapping of the entire epithelium from base to surface can provide in-depth information regarding the process of malignant transformation. An earlier study by our group has demonstrated a difference between the epithelium and stroma, especially in the collagen content.<sup>23</sup> Also, a recent study by L. J. Cals Froukje et al. has shown that the spectra of basal, loose connective tissue and dense connective tissue are different.<sup>22</sup> As earlier studies have already demonstrated the difference between epithelium and stroma, the present study was undertaken for a site-specific and in-depth study of normal epithelium and tumor histological features through Raman mapping. Histopathology “vis-à-vis” Raman maps of normal and cancerous tissues has been discussed in the paper.

## 2 Material and Methodology

### 2.1 Sample Handling

Tissue specimens were collected from resection material of OSCC, patients who had undergone surgical procedures at ACTREC, TMC, Navi Mumbai. Twenty tissues samples each of tumor and normal mucosa (~3.5 cm margin) were collected from 20 patients. Adjacent 5 and 16  $\mu\text{m}$  thick sections were obtained. The 5  $\mu\text{m}$  sections were stained with HE for histopathological evaluation. These sections were histopathologically verified by pathologist and probing areas were identified for conducting experiments. Then, the 16  $\mu\text{m}$  unfixed, unstained tissue sections were used for Raman spectral acquisition without further treatment.

### 2.2 Data Acquisition

Raman spectra of tissue sections were acquired using WITec Raman alpha300 R (WITec GmbH) confocal Raman imaging system. The instrument was calibrated for spectra using an argon mercury lamp. The microscope is equipped with XYZ piezo-scan stage, and a computer controlled sample stage with a maximum scan area of  $200 \times 200 \times 20 \mu\text{m}$  respectively, which enables automatic scanning of the sample. For excitation at 8 mW power, a 532 nm Nd:YAG laser was focused by a  $50\times$  (0.55 NA, Zeiss) objective onto the sample and resultant Raman signals were detected using a 300 mm spectrograph with 600 g/mm grating coupled with a charged couple device (CCD). Raman spectra were obtained using a pointwise technique from the predefined grid on tissue sections with a resolution of 4  $\mu\text{m}$ . Raman spectra were acquired in the 0 to

3600  $\text{cm}^{-1}$  region with an integration time of 5 s/spectrum. Parameters were kept constant for all measurements. Twenty Raman mapping experiments were performed on the 20 tissue sections. In pathologically verified normal tissue sections, the stratification of the epithelium remains same across the tissue section. In order to probe the entire epithelium, two adjacent maps were acquired covering the area of  $160 \times 60 \mu\text{m}/\text{map}$ . Then these two adjacent maps were combined. This was done due to the limited scan size of the instrument. In case of malignant samples, the scan size was varied from  $60 \times 60$  to  $140 \times 140 \mu\text{m}/\text{map}$  depending on the probing area. About 19,200 spectra/map for normal epithelium and 3600 to 19600 spectra/map for tumor sections were collected.

### 2.3 Data Processing and Analysis

Raman maps were constructed using WITec project plus software. The raw spectra were acquired from unstained and unfixed cryosection of oral buccal mucosa in the range of 0 to 3600  $\text{cm}^{-1}$  as a predefined hyperspectral cube. Basic preprocessing steps were carried out which included correction for CCD response and subtraction of background signals. Further, spectra were interpolated in the finger-print region from 500 to 1800  $\text{cm}^{-1}$ . First-derivative spectra were used to minimize the influence of a slow moving fluorescence background (Savitzky–Golay method, window size-3), followed by vector normalization.<sup>8–10</sup> These first-derivative spectra were subjected to multivariate statistical tool *K*-means cluster analysis (KCA) for generation of Raman maps. KCA is an algorithm used to classify/group spectra based on features into *K* number of groups, and is done by minimizing the sum of the squares of the distances between the data and the corresponding cluster centroid. Each cluster reflects the distribution of biomolecules in a sample and assigns it a distinguishing pseudocolor. This approach has been routinely used for imaging so that large spectral data acquired during experiments can be easily handled. KCA clusters were chosen so as to match histopathological structures present in tissue sections which were examined by pathologists. In order to ensure the robustness of the methodology, the standardized protocol was applied on the remaining nine sections and, in turn, was correlated with HE-stained tissue sections under the guidance of the pathologist. In normal maps, the superficial layer, intermediate layer, basal layer, and stroma were identified and correlated with four KCA clusters. In the case of tumors, three clusters were used for annotations of tumors cells, inflammatory cells, and stromal region. WITec project plus software has a feature that allows extraction of cluster average spectra of the map from any of the above mentioned preprocessing steps. In order to understand spectral variations among different histopathological structures, we have extracted the cluster average just prior to derivatization for each of annotated histopathological structures, from 10 normal and 10 tumor sections. The mean spectra from cluster averages of same histopathological structure were computed and baseline corrected by fitting the fifth order polynomial function, followed by smoothing (Savitzky–Golay method, window size-3) and vector normalization steps. These spectra were utilized for spectral comparisons and difference spectra analyses. The robustness of the approach is also tested by principal component analysis (PCA) carried out on derivatized average spectra extracted from all pixels identified as one histopathological structure (e.g., basal, intermediate, etc.) by KCA. These average spectra from different samples were used as input for PCA. These

cluster averages spectra were subjected to PCA to find patterns and trends among the spectra.

### 3 Results and Discussion

The present Raman mapping study was undertaken for in-depth and site-specific analysis of oral normal and tumor tissues, which can provide an insight into the biochemical alterations of the mucosa.

#### 3.1 Correlation between Raman Maps and Histopathological Structures

The unstained pictograph, H&E stained image and corresponding Raman map of representative normal tissue sections are shown in Figs. 1(a)–1(c). Three stratified layers of epithelium namely—S (superficial), I (intermediate), B (basal) and ST (stroma) were identified on H&E stained sections [Fig. 1(B)] and the corresponding Raman maps [Fig. 1(C)]. These were annotated as cluster 1 for superficial, cluster 2 for intermediate, and cluster 3 as the basal layer, as shown in Fig. 1C(a). Along with the three layers in Fig. 1C(b–c), the ST as cluster 4 was also identified on Raman maps.

The unstained pictograph, H&E stained image, and corresponding Raman map of representative poorly differentiated tumor tissue sections are shown in Figs. 2(a)–2(c). Three different tissue components, TU (tumor), IN (inflammatory), and TST (tumor stroma), were identified on H&E stained sections [Fig. 2(B)] and the corresponding Raman maps [Fig. 2(C)]. These were annotated as cluster 1 for tumor cells, cluster 2 for inflammatory cells, and cluster 3 as stroma, Fig. 2C(a).

#### 3.2 Mean Spectral Analysis

A total of 58 reference spectra (28 normal and 30 tumors) were extracted from six specific histopathological features. Baseline

corrected cluster average spectra of normal and tumor sections were computed and are shown in Figs. 3 and 4. All histological structures of normal and malignant tissue sections exhibit spectral features of biomolecules such as protein, nucleic acid, etc. Other notable features are of enhanced cytochrome bands at  $\sim 750$ , 1135, 1315, and  $1595\text{ cm}^{-1}$  which can be due to the resonance effect (Figs. 3 and 4).<sup>24,25</sup>

In the case of normal sections, protein bands at amide I ( $\sim 1660\text{ cm}^{-1}$ ),  $\delta\text{CH}_2$  bending ( $\sim 1454\text{ cm}^{-1}$ ), and amide III ( $\sim 1240\text{ cm}^{-1}$ ) were observed in the mean spectra of superficial as well as intermediate layers [Figs. 3(a) and 3(b)]. DNA bands at  $\sim 720$ , 782, 1096,  $1340\text{ cm}^{-1}$  were observed in the mean spectrum of the basal layer [Fig. 3(c)]. In the case of tumor sections, DNA and predominant protein bands were observed, as indicated by amide I band ( $1660\text{ cm}^{-1}$ ),  $\delta\text{CH}_2$  bending ( $\sim 1454\text{ cm}^{-1}$ ), and amide III ( $\sim 1240\text{ cm}^{-1}$ ), Fig. 4(a). The bands at  $\sim 1162$  and  $1525\text{ cm}^{-1}$  observed in the inflammatory cells indicate the presence of carotenoids [Fig. 4(b)]. Carotenoids are strong Raman scatterers, especially when resonantly excited around 400 to 500 nm and are known to be effective quenchers of singlet oxygen and radicals, which is important in cancer etiology. Further, it was observed that tumor stroma shared similar spectral features with that of tumor cells [Figs. 4(a)–4(c)].

As explained earlier, the non-keratinized stratified squamous epithelium comprises three layers—basal, intermediate, and superficial. The basal layer contains the stem cells necessary for regeneration of this renewable tissue and is made up of a single layer of cuboidal cells. As the cells migrate from the basal to the superficial layer, the cells mature and finally desquamate after reaching the surface.<sup>4</sup> Since the basal layer is actively involved in cell division for the continuous renewal of the epithelium, the presence of DNA bands in the basal layer can be explained. Toward the superficial layer, loss of DNA-related bands and dominance of protein-related bands

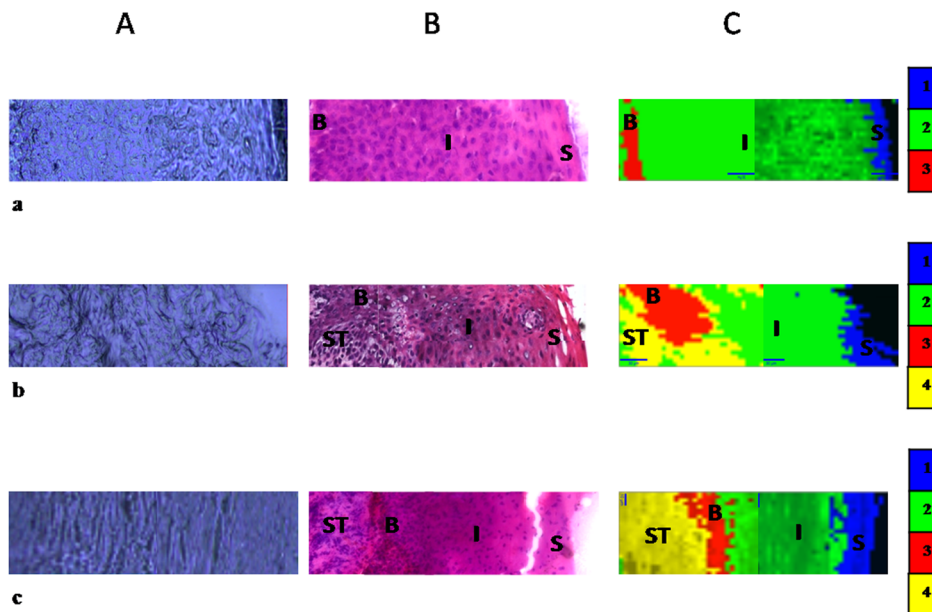


**Fig. 1** Raman maps—correlation between the unstained tissue section, HE-stained section, and Raman images. Three normal tissue section (a–c), Panel (A)  $16\text{ }\mu\text{m}$  unstained tissue (original magnification  $50\times$ ). (B)  $5\text{ }\mu\text{m}$  H&E stained tissue (original magnification  $40\times$ ) for histopathological correlation. (C) The pseudocolor Raman map (original magnification  $50\times$ ) based on KCA was used to identify, cluster 1 as superficial layer (S), cluster 2 as intermediate layer (I), cluster 3 as basal layer (B), and cluster 4 as stroma (ST).

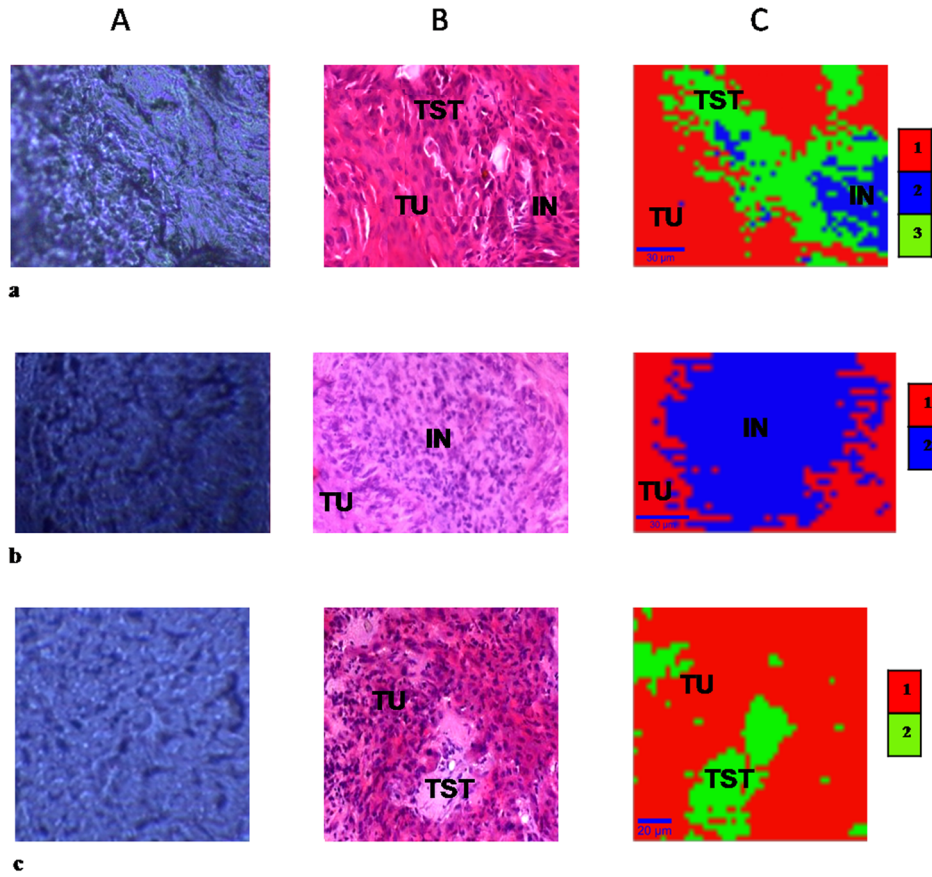


**Fig. 2** Raman maps—correlation between the unstained tissue section, HE-stained section and Raman images. Three tumor tissue section (a–c), Panel (A) 16  $\mu\text{m}$  unstained tissue (original magnification 50 $\times$ ). (B) 5  $\mu\text{m}$  H&E stained tissue (original magnification 40 $\times$ ) for histopathological correlation. (C) The pseudocolor Raman map (original magnification 50 $\times$ ) based on KCA was used to identify, cluster 1 as tumor cells (TU), cluster 2 as inflammatory cells (IN) and cluster 3 as stroma (TST).

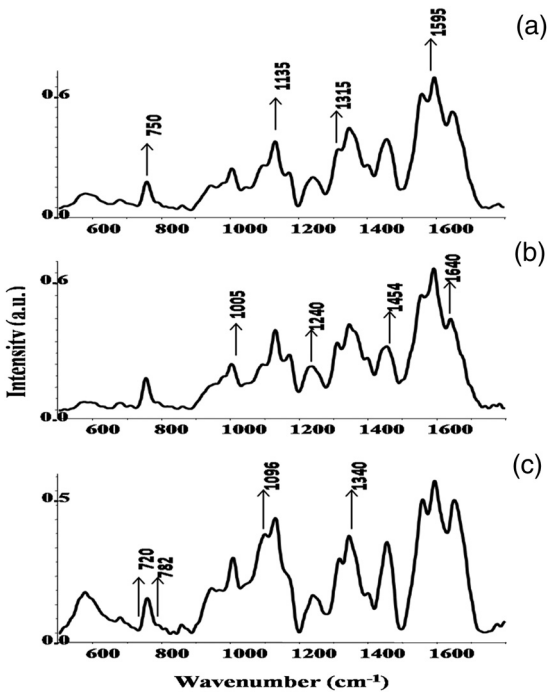


**Fig. 3** Mean spectra—normal stratified epithelium (a) superficial, (b) intermediate, and (c) basal.

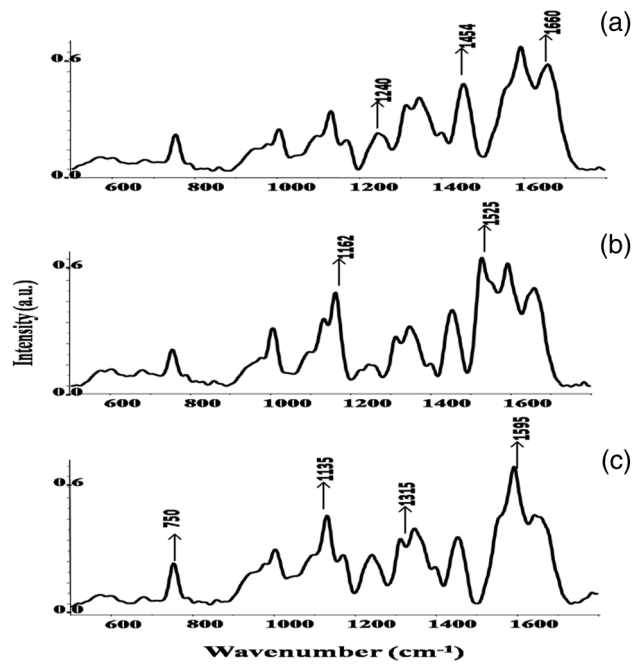


**Fig. 4** Mean spectra—tumor tissue sections (a) tumor cells (b) inflammatory (c) stroma.

were observed. This can be due to desquamation of cells towards the superficial layer. This observation corroborates with the earlier reports.<sup>16,22</sup>

OSCC is characterized by structural loss in the stratification of the epithelium. Further, it leads to subsequent invasion and infiltration of malignant epithelial cells into the connective tissue. It is a known fact that tumorigenesis is accompanied by uncontrolled cell division. Increased cell division has a requirement of increased protein, which may explain predominant protein bands in tumor cells; along with DNA bands, as the cells are in a highly proliferative state.<sup>4,26</sup> The basic function of the inflammatory cells is to elicit the immune response. It is a known fact that carotenoids, which act as antioxidants, are present in gall bodies of lymphocytes. This may explain their presence in inflammatory cells in tumor sections.<sup>27</sup> As most of the sections under consideration are from aggressive, poorly differentiated carcinomas, tumor stroma and tumor cells are in intimate association with each other.<sup>26</sup> Similar spectral features were, therefore, observed for tumor cells and stroma.

### 3.3 Difference Spectral Analysis

To understand spectral variations, difference spectra were computed (Figs. 5 and 6). Subtraction of mean spectra is one of the conventional ways of looking at spectral differences. It can provide differences over the selected spectral range and can help in understanding the moieties that are modified. In normal tissues, the basal layer is the only layer that contains actively dividing cells. Moreover, cell division in this layer is different from that of the diseased condition.<sup>4</sup> Hence, the basal layer was considered as the control to compute difference spectra. In order to understand the differences among various histopathological structures, difference spectra were computed by subtracting the mean control spectrum (basal layer) from the mean spectra of (i) superficial, (ii) intermediate, (iii) tumor, (iv) inflammatory cells, and (v) tumor stroma. As shown in Figs. 5 and 6, all positive peaks correspond to histopathological features of the superficial layer, intermediate layer, tumor cells, inflammatory cells, tumor stroma, while the negative bands are from the basal layer.

In the difference spectrum of the superficial layer—control [Fig. 5(a)], the positive bands from fatty acids is at  $\sim 1262$ ,  $1304\text{ cm}^{-1}$ , lipids = CH bending ( $\sim 980\text{ cm}^{-1}$ ),  $\delta\text{CH}_3$  symmetric

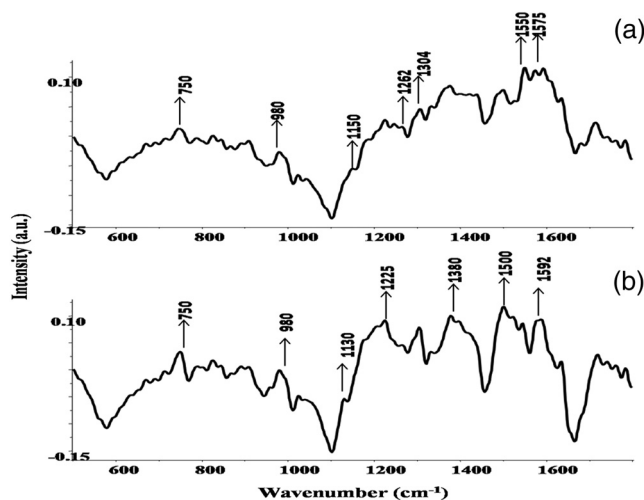


**Fig. 5** Difference spectra (a) superficial minus basal and (b) intermediate minus basal.

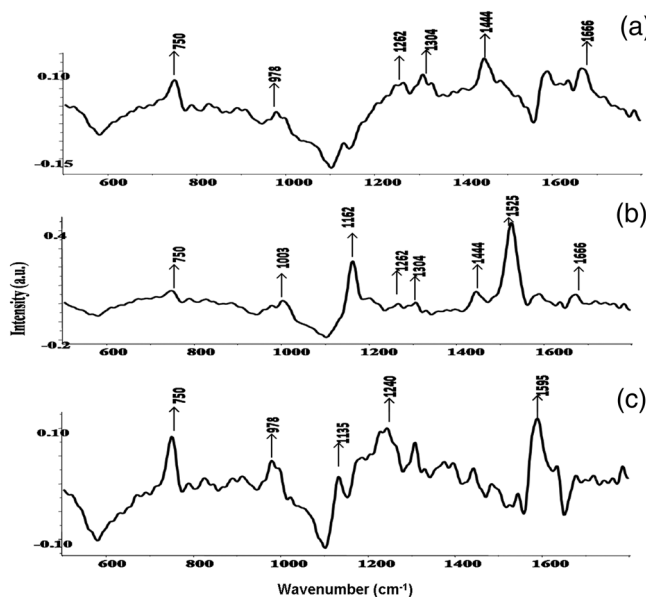


**Fig. 6** Difference spectra (a) tumor cells minus basal, (b) inflammatory minus basal, and (c) stroma minus basal.

( $\sim 1380$ ) along with heme  $\sim 1550$ ,  $1574\text{ cm}^{-1}$  with respect to the control were observed, suggesting the predominance of lipids in the superficial layer. In the difference spectrum of the intermediate layer—control, cytochrome bands were observed indicated by positive bands at  $\sim 750$ ,  $1130$ , and  $1595\text{ cm}^{-1}$  [Fig. 5(b)]. This may imply intensity variations of cytochromes in the intermediate layer with respect to the control. It is a known fact that in the superficial layer of normal epithelium, apoptosis is in the execution phase. Due to this, phospholipids/phosphatidylserines are expressed on the outer layer of the cells. This may lead to predominant lipid bands in the superficial layer with respect to the basal layer.<sup>6</sup> This observation corroborates with earlier reports.<sup>16,22</sup> An observed cytochrome predominance in the intermediate layer can be attributed to initiation of the partial activation of apoptosis pathway in this layer, which ultimately results in cell desquamation at the surface of the epithelium.<sup>28</sup>

The positive bands of proteins at amide III ( $\sim 1225$ ,  $1262\text{ cm}^{-1}$ ),  $\delta\text{CH}_2$  bending ( $\sim 1444\text{ cm}^{-1}$ ), amide I ( $\sim 1666\text{ cm}^{-1}$ ), fatty acids bands at  $\sim 1263$  and  $1305\text{ cm}^{-1}$ , and =CH bending lipids ( $\sim 980\text{ cm}^{-1}$ ) were observed in the difference spectrum of tumor cells—control [Fig. 6(a)], which suggest tumor cells are rich in proteins as well as lipids with respect to the control. Along with proteins bands, fatty acids bands ( $\sim 1263$  and  $1305\text{ cm}^{-1}$ ) were observed in inflammatory cells—control spectrum, suggesting an abundance of fatty acids and proteins in inflammatory cells as shown in Fig. 6(b). Cytochrome bands were observed in tumor stroma—control spectrum [Fig. 6(c)]. Gene mutations that cause aberrant uncontrolled cell division subsequently lead to changes in cellular biochemistry. This cell division is different from the controlled cell division of the rapidly dividing basal cell layer. This leads to increased requirements of proteins of cells, which can be seen in the difference spectrum of tumor cells—control [Fig. 6(a)]. Tumor cells also express high levels of fatty-acid synthase and undergo significant endogenous fatty-acid synthesis for membrane biogenesis. Due to this, fatty acids bands were also observed in tumor cells in control difference spectrum [Fig. 6(a)].<sup>29</sup> Lipid bodies (LBs) present in inflammatory

cells are associated with the elicitation of the immune response. LBs are dynamic and functionally active organelles involved in a variety of functions such as lipid metabolism, cell signaling, and inflammation. In these cells, LBs contribute to the genesis of inflammatory mediators and have been considered structural markers of inflammation.<sup>30</sup> This explains the presence of lipids in the difference spectrum of inflammatory—control, as shown in Fig. 6(b). LB also consists of specific structural proteins, the PAT family of proteins found at the circumferential rim of LBs.

Moreover, a number of small GTPases of the Rab family, considered critical regulators of vesicular traffic and organelle interaction, and a variety of other proteins are present in LBs. The high protein content in LBs explains the presence of proteins in the difference spectrum of inflammatory—control [Fig. 6(b)].<sup>30</sup> Similarly, cytochrome bands were observed in tumor stroma—control spectrum as shown in Fig. 6(c). This can be due to the fact that cytochrome mediates synthesis of intermediate metabolites hydroxyeicosatetraenoic acids or epoxyeicosatrienoic

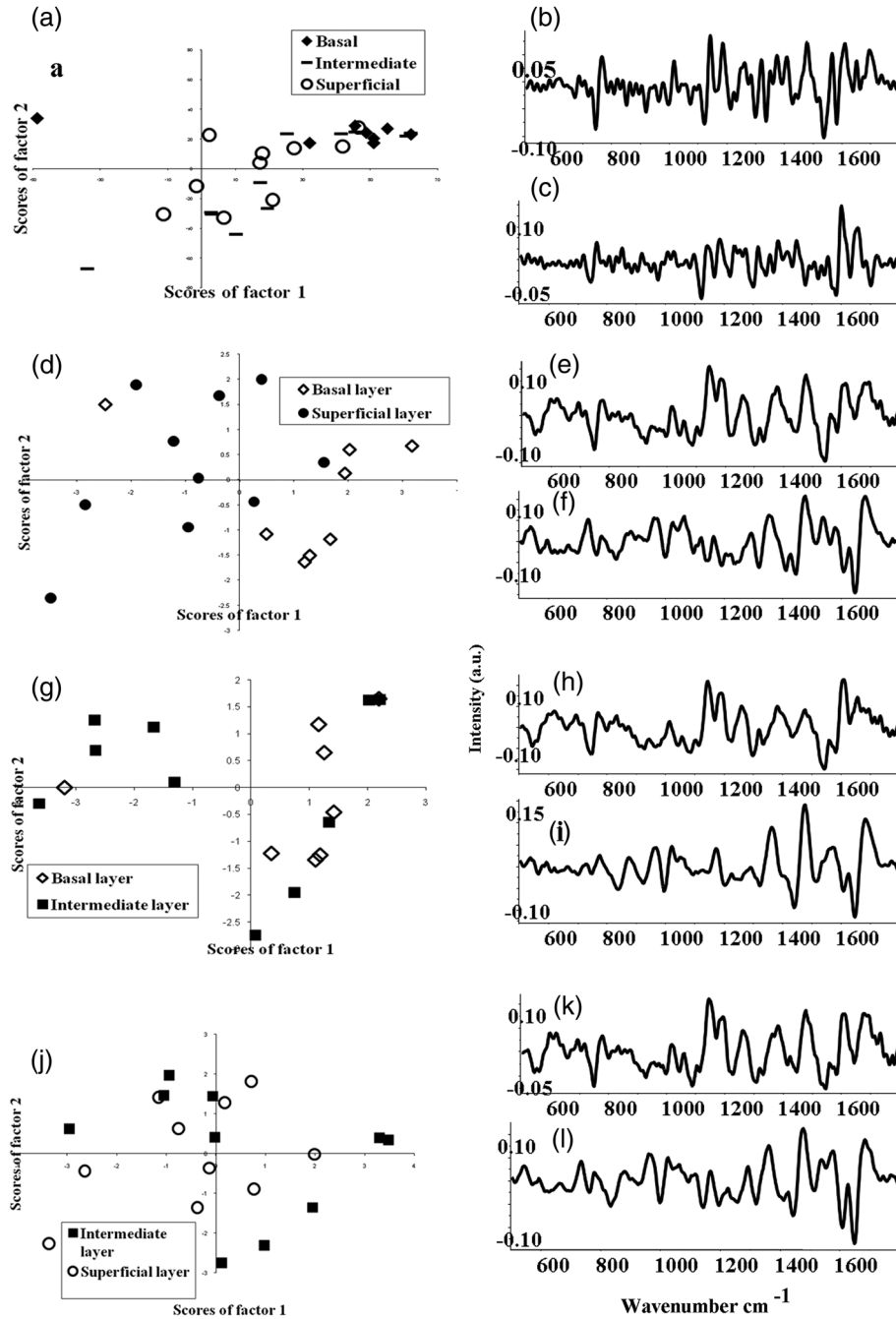


**Fig. 7** Scatter plot of PCA of (a) all three layers of basal (◆), intermediate (-), and superficial (○), (b and c) loadings factor 1 and 2 for scatter plot of all three layers (d) basal (◇) versus superficial (●) (e and f) loadings factor 1 and 2 for scatter plot of basal versus superficial layer (g) Intermediate (■) versus basal (◇), (h-i) loadings factor 1 and 2 for scatter plot of intermediate versus basal, (j) intermediate (■) versus superficial (○) for normal tissue sections and (k and l) loadings factor 1 and 2 for scatter plot of intermediate versus superficial.

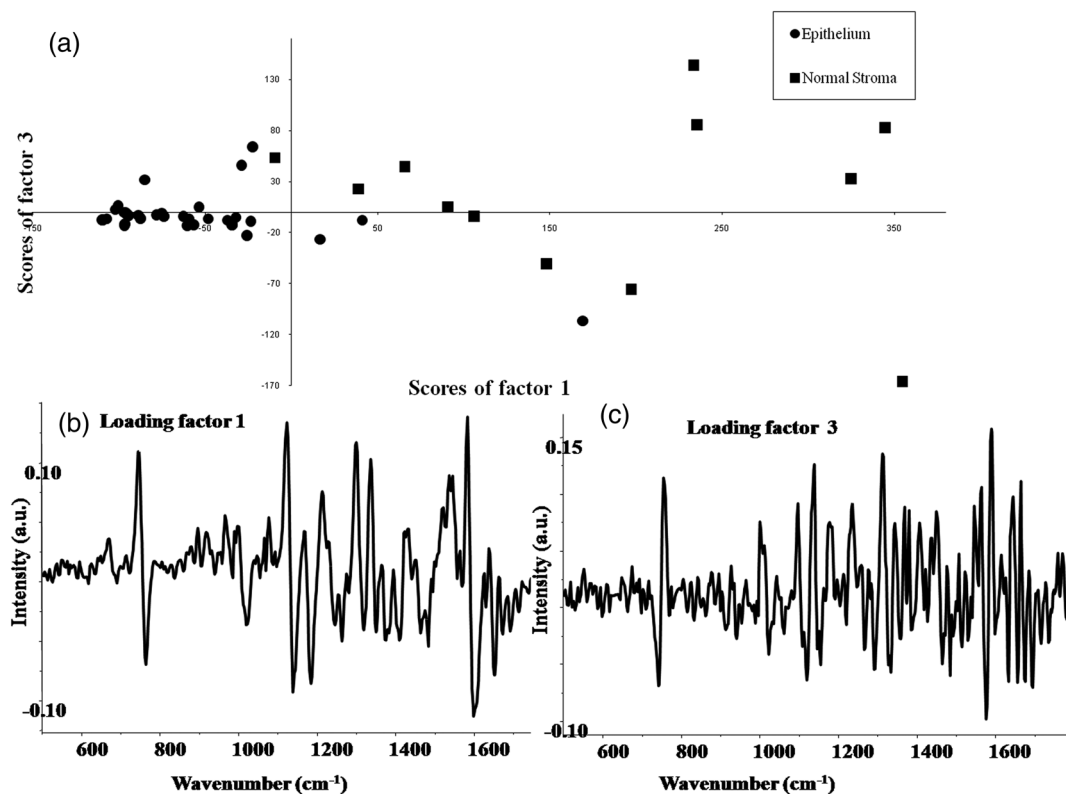


**Fig. 8** (a) Scatter plot of PCA of normal epithelium (●) and normal stroma (■), (b) loading factor 1, and (c) loading factor 3.

acids of the arachidonic acid metabolism in the stroma. These metabolites are involved in the modulation of stromal processes, such as angiogenesis and inflammation, which can support tumor progression.<sup>31</sup> The spectra are assigned based on the available literature.<sup>16,22,23–25</sup>

### 3.4 Principal Component Analysis

PCA was carried out to obtain trends and patterns in annotated regions of normal and tumor tissue sections. We have carried out the PCA in three different steps: (1) all three layers of the epithelium, (2) normal epithelium and normal stroma, and (3) various cellular regions of normal and tumor section.

It is a known fact that premalignant or carcinoma *in-situ* conditions are also associated with changes in the superficial as well as intermediate layers. In order to understand the variations during (pre)-malignant progression, it is important to identify the biochemical variations among stratified layers of normal epithelium. PCA was carried out for (1) all layers of normal epithelium [Figs. 7(a)–7(c)] and (2) pair wise approach i.e., superficial versus basal, intermediate versus basal, and intermediate versus superficial [Figs. 7(d)–7(l)]. Findings suggest that basal and superficial layers of the epithelium can be separated [Figs. 7(a) and 7(d)]. Profiles of the principal components (PCs) also known as factor loadings can provide vital clues on biochemical variations. The loading factors of the principal component [PC1, Fig. 7(b)] show the presence of cytochrome bands at  $\sim 750$ ,  $1135$ ,  $1315$  and  $1595$   $\text{cm}^{-1}$  and fatty acid bands  $\sim 1262$ ,  $1304$   $\text{cm}^{-1}$ . In the second component, Fig. 7(c) suggests DNA  $\sim 720$ ,  $782$ ,  $1096$ ,  $1340$   $\text{cm}^{-1}$ . Similarly, the fatty acid bands  $\sim 1262$ ,  $1304$   $\text{cm}^{-1}$  were observed in PC1 [Fig. 7(e)] and DNA  $\sim 720$ ,  $782$ ,  $1096$ ,  $1340$   $\text{cm}^{-1}$  in PC2

[Fig. 7(f)], which explains the discrimination between the superficial and basal layers. These findings can be explained on the basis that the basal layer is the only layer of the stratified epithelium which is actively involved in cell division, whereas the superficial layer consists of flattened cells that finally desquamate. This difference in cell turn over with a subsequent change in cell biochemistry explains this classification.

The spectra of the intermediate layer show misclassification with both layers i.e., superficial and basal layers [Figs. 7(a), 7(g), 7(j)], which can be attributed to the fact that the intermediate layer is the transitional layer between the cells of origin from the basal to the gradual flattening of the superficial layer. PC1 and 2 of this PCA [Figs. 7(h–i) and 7(k–l)] are rich in cytochromes  $\sim 750$ ,  $1135$ ,  $1315$  and  $1595$   $\text{cm}^{-1}$  and proteins amide III ( $\sim 1262$   $\text{cm}^{-1}$ ),  $\delta\text{CH}_2$  bending ( $\sim 1444$   $\text{cm}^{-1}$ ), and amide I ( $\sim 1666$   $\text{cm}^{-1}$ ). As similar features in PCs were observed, misclassification of intermediates as basal and superficial can be explained.

Further, PCA was carried out between the spectra of stromal and epithelial regions and findings suggest that these two regions can be separated in normal tissues, Fig. 8(a). This observation can be attributed to the fact that stroma is rich in proteins (collagen) in comparison to epithelium.<sup>4,26</sup> The loading plots of factors 1 and 2 that lead to delineation among epithelium and normal stroma are presented in Figs. 8(b) and 8(c). The first PC (PC1) shows the predominant bands of cytochrome at  $\sim 750$ ,  $1135$ ,  $1315$  and  $1595$   $\text{cm}^{-1}$ . In the second component (PC2), the main peak features corresponding to amide I band ( $1660$   $\text{cm}^{-1}$ ),  $\delta\text{CH}_2$  bending ( $\sim 1454$   $\text{cm}^{-1}$ ), and amide III ( $\sim 1240$   $\text{cm}^{-1}$ ) were observed.

PCA was also carried out among the spectra extracted from various cellular regions. In this case, tumor cells gave a separate

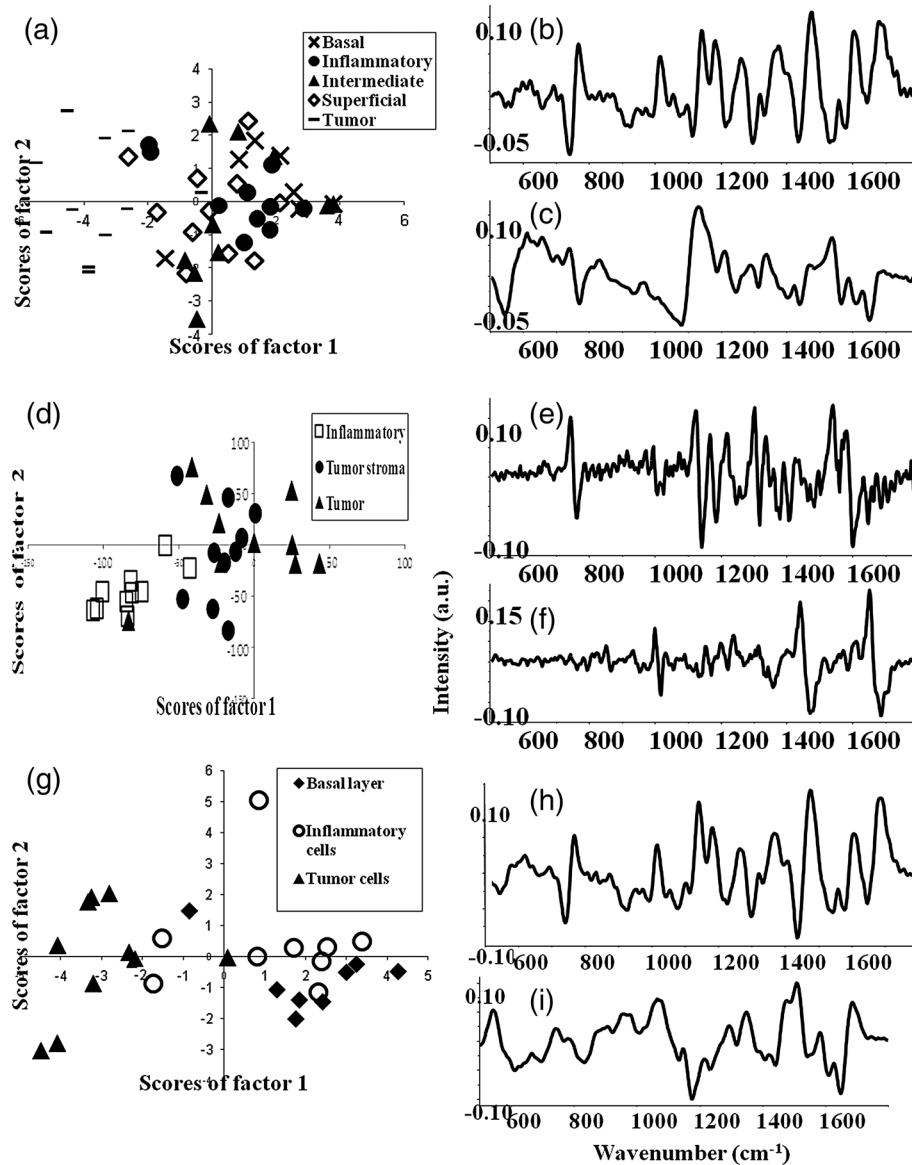


**Fig. 9** (a) Scatter plot of all cells—tumor cells (-), inflammatory cells (●), basal layer (x), intermediate layer (▲), and superficial layer (◊), (b and c) loadings factor 1 and 2 for scatter plot of all cells, (d) scatter plot of three zones of tumor sections—tumor cells (▲), inflammatory cells (◻), and tumor stroma (●), (e and f) loadings factor 1 and 2 for scatter plot of three zones of tumor sections, (g) scatter plot of PCA of basal layer (◆), inflammatory cells (○), and tumor cells (▲) and (h and i) loadings factor 1 and 2 for scatter plot of basal, inflammatory, and tumor cells.

cluster while the spectra of inflammatory cells show an overlap with superficial cells, Fig. 9(a). Lipid rich features in both groups can explain this misclassification among inflammatory cells and the superficial layer. The first principal component [PC1, Fig. 9(b)] has cytochrome at  $\sim 750$ , 1135, 1315 and  $1595\text{ cm}^{-1}$ , whereas the second component [PC2, Fig. 9(c)] corresponds to fatty acids bands at  $\sim 1262$ ,  $1304\text{ cm}^{-1}$  and carotenoids  $\sim 1162$  and  $1525\text{ cm}^{-1}$ . A PCA study was also carried among the three zones in tumor tissue sections, namely tumor cells, inflammatory cells, and tumor stroma [Fig. 9(d)]. In the PCs, the predominance of cytochrome was at  $\sim 750$ , 1135, 1315 and  $1595\text{ cm}^{-1}$  in the first principal component [PC1, Fig. 9(e)] and of carotenoids  $\sim 1162$  and  $1525\text{ cm}^{-1}$  in the second component [PC2, Fig. 9(f)]. It was observed that inflammatory cells could be differentiated from tumor cells

and tumor stroma. This discrimination could be due to the fact that the origins of the two types of cells, i.e., tumor and inflammatory cells are different. The principal function of inflammatory cells is to phagocytosis, whereas that of tumor cells is division. This difference in function leads to a variation in biochemical composition for two cell types resulting in their discrimination. The tumor cells and tumor stroma show misclassification among themselves as shown in Fig. 9(d). As most of the sections under consideration are that of aggressive poorly defined carcinoma resulting in the intermixing of the tumor with the stroma, such misclassifications cannot be ruled out. Inflammatory conditions like lichen planus are difficult to differentiate from premalignant conditions (leukoplakia). This necessitates identifying inflammatory cells from tumors and basal (normal) cells. Thus, PCA was also carried out for tumor,

inflammatory and basal cells as shown in Fig. 9(g). The first principal component [PC1, Fig. 9(h)] has major bands that correspond to proteins amide I band  $1660\text{ cm}^{-1}$ ,  $\delta\text{CH}_2$  bending  $\sim 1454\text{ cm}^{-1}$  and amide III  $\sim 1240\text{ cm}^{-1}$ . In the second component [PC2, Fig. 9(i)], the main peak features correspond to DNA at  $\sim 720, 782, 1096, 1340\text{ cm}^{-1}$ . It was observed that inflammatory cells and the basal layer which are in close proximity could be due to the PC2 which corresponds to DNA since they are nonmalignant groups. Still, PCA suggests classification among all the three groups. This can be attributed to the fact that tumor cells have uncontrolled cell division which is different from the controlled cell division of the basal layer. Similarly, inflammatory cells elicit the immune response and have a different biochemical composition compared to both tumor cells and basal layer.

Fiberoptic Raman spectroscopic studies have successfully demonstrated that normal and pathological conditions along with various confounding factors associated with oral cancers can be identified.<sup>8–11</sup> Raman microspectroscopy is a valuable research technique for tissue biology and can provide site-specific molecular composition. The present Raman mapping study was undertaken for in-depth and site-specific analysis of normal and tumor tissues. Our study has suggested that the layer wise stratification of the epithelium and tumor regions can be achieved by Raman mapping. In addition, maps also can shed light on the biochemical/molecular composition of a tissue compared to histopathological images which mostly depict morphology. Thus, Raman maps are also useful in understanding biochemical alterations of the mucosa during disease progression, which in turn can be used for defining new treatment strategies and the development of new detection methodology for early detection of oral cancer. Large scale validation studies with an increased sample size of normal, premalignant and tumor tissues section will be helpful in understanding biochemical changes associated with tumor transformation. In the current scenario, Raman mapping cannot replace the HE examinations due to limitations like prolonged spectral acquisition as well as data analysis time. With prospective development of methods such as coherent anti-stokes Raman spectroscopy and stimulated Raman spectroscopy, which can dramatically reduce spectral acquisition times, Raman mapping can emerge as an adjuvant technique along with routine HE examination, with the added advantage of providing molecular insights.

### Acknowledgments

This work was carried out under women scientist fellowship-B scheme project no: SSD/SS/026, Department of Science and Technology, Government of India. One of the authors, Isha Behl, thanks the Department of Science and Technology, Government of India, for a fellowship.

### References

1. World Health Organization: The GLOBOCAN 2012 database, <http://globocan.iarc.fr> (28 October 2014).
2. R. Dikshit et al., "Cancer mortality in India: a nationally representative survey," *Lancet* **378**(9828), 1807–1816 (2012).
3. N. B. Ramachandra, "The hierarchy of oral cancer in India," *Int. J. Head Neck Surg.* **3**(3), 143–146 (2012).
4. G. Kumar, *Orban's Oral Histology and Embryology*, 12th ed., Elsevier, India (2009).
5. D. C. G. De Veld et al., "The status of in vivo autofluorescence spectroscopy and imaging for oral oncology," *Oral Oncol.* **41**, 17–31 (2005).

6. C. Kendall et al., "Vibrational spectroscopy: a clinical tool for cancer diagnostics," *Analyst* **134**, 1029–1045 (2009).
7. A. Nijssen et al., "Towards oncological application of Raman spectroscopy," *Biophoton.* **2**, 29–36 (2009).
8. S. P. Singh et al., "In vivo Raman spectroscopy for oral cancers diagnosis," *Proc. SPIE* **8219**, 82190K (2012).
9. S. P. Singh et al., "In vivo Raman spectroscopic identification of pre-malignant lesions in oral buccal mucosa," *J. Biomed. Opt.* **17**(10), 105002 (2012).
10. S. P. Singh et al., "In vivo Raman spectroscopy of oral buccal mucosa: a study on malignancy associated changes (MAC)/cancer field effects (CFE)," *Analyst* **138**, 4175–4182 (2013).
11. H. Krishna et al., "In vivo Raman spectroscopy for detection of oral neoplasia: a pilot clinical study," *J. Biophotonics* **7**(9), 690–702 (2014).
12. G. J. Puppels et al., "Studying single living cells and chromosomes by confocal Raman microspectroscopy," *Nature* **347**, 301–303 (1990).
13. M. Gniadecka et al., "Diagnosis of basal cell carcinoma by Raman spectroscopy," *J. Raman Spectrosc.* **28**, 125–129 (1997).
14. A. Nijssen, "Discriminating basal cell carcinoma from its surrounding tissue by Raman spectroscopy," *J. Invest. Dermatol.* **119**(1), 64–69 (2002).
15. S. Koljenovic et al., "Detection of Meningioma in dura mater by Raman spectroscopy," *Anal. Chem.* **77**(24), 7958–7965 (2005).
16. S. Koljenovic et al., "Raman microspectroscopic mapping studies of human bronchial tissue," *J. Biomed. Opt.* **9**(6), 1187–1197 (2004).
17. S. Koljenovic et al., "Discriminating vital tumor from necrotic tissue in human glioblastoma tissue samples by Raman spectroscopy," *Lab. Invest.* **82**(10), 1265–1277 (2002).
18. A. Beljebbar et al., "Identification of Raman spectroscopic markers for the characterization of normal and adenocarcinomatous colonic tissues," *Crit. Rev. Oncol. Hematol.* **72**(3), 255–264 (2009).
19. K. M. Tan, C. S. Herrington, and C. T. Brown, "Discrimination of normal from pre-malignant cervical tissue by Raman mapping of de-paraffinized histological tissue sections," *J. Biophotonics* **4**(1–2), 40–48 (2011).
20. G. Shetty et al., "Raman spectroscopy: elucidation of biochemical changes in carcinogenesis of oesophagus," *Br. J. Cancer* **94**, 1460–1464 (2006).
21. C. Krafft et al., "Raman and FTIR imaging of lung tissue: methodology for control samples," *Vib. Spectrosc.* **46**, 141–149 (2008).
22. L. J. C. Froukje et al., "Method development: Raman spectroscopy based histopathology of oral mucosa," *J. Raman Spectrosc.* **4318**, 1–10 (2013).
23. C. M. Krishna et al., "Micro-Raman Spectroscopy for Optical Pathology of Oral Squamous Cell Carcinoma," *Appl. Spectrosc.* **58**(9), 107–114 (2004).
24. F. S. Parker, *Applications of Infrared, Raman and Resonance Raman Spectroscopy in Biochemistry*, Plenum Press, New York and London (1983).
25. C. Scalfi-Happ et al., "Confocal Raman microscopy as a diagnostic tool for investigation of living neuroblastoma tumour cells," *Med. Laser Appl.* **22**, 157–164 (2007).
26. V. Kumar, A. K. Abbas, and N. Fausto, *Robbins and Cotran Pathologic Basis of Disease*, 7th ed., Elsevier (2005).
27. T. C. B. Schut et al., "Intracellular carotenoid levels measured by Raman microspectroscopy: comparison of lymphocytes from lung cancer patients and healthy individuals," *Int. J. Cancer* **74**, 20–25 (1997).
28. M. A. Birchall et al., "Apoptosis in normal epithelium, premalignant and malignant lesions of the oropharynx and oral cavity: a preliminary study," *Oral Oncol. Eur. J. Cancer* **31B**, 380–383 (1995).
29. F. P. Kuhajda, "Fatty-acid synthase and human cancer: new perspectives on its role in tumor biology," *Nutrition* **16**, 202–208 (2000).
30. R. C. N. Melo et al., "Lipid bodies in inflammatory cells: structure, function, and current imaging techniques," *J. Histochem. Cytochem.* **59**(5), 540–556 (2011).
31. D. Panigrahy et al., "Cytochrome P450-derived eicosanoids: the neglected pathway in cancer," *Cancer Metastasis Rev.* **29**, 723–735 (2010).

Biographies of the authors are not available.